Electronic Supplementary Information

Aromatic cation-π induced multifluorescence tunable two-dimensional co-assemblies for encoded information security

Zhao Gao,[‡a] Jianxiang Sun [‡a], Lulu Shi[a], Wei Yuan[b], and Wei Tian[*a]*

[a]Shaanxi Key Laboratory of Macromolecular Science and Technology, Xi'an Key Laboratory of Hybrid Luminescent Materials and Photonic Device, MOE Key Laboratory of Material Physics and Chemistry under Extraordinary Conditions, School of Chemistry and Chemical Engineering, Northwestern Polytechnical University, Xi'an 710072, P. R. China. E-mail: Wei Tian (happytw_3000@nwpu.edu.cn)
[b]Department of Chemistry, National University of Singapore 3 Science Drive 3, Singapore 117543, Singapore.

Contents

1.	*Materials and methods*	S2
2.	*Supplementary Figures*	S5
3.	*Synthetic routes to the targeted monomer*	S19
4.	*References*	S22

1. Materials and methods

Reagents and reactants: 9,10-Diiodoanthracene[1] was synthesized according to the previously reported literatures. Other reagents and solvents used in the experiments were purchased from commercial sources without further purification.

Measurements: ^{1}H NMR, ^{13}C NMR, spectra were obtained from Bruker Avance 400 instruments. High-resolution electrospray ionization mass spectra (HR-ESI-MS) were obtained on a Bruker Esquire 3000 plus mass spectrometer equipped with an ESI interface and ion trap analyzer. UV–Vis absorption spectra were performed on a Shimadzu UV-2600 spectrometer. Fluorescence spectra were recorded on a Hitachi F-4600 FL spectrophotometer. The time-resolved fluorescence lifetime experiments were performed with an Edinburgh FLS980 transient steady-state fluorescence spectrometer. Quantum yields were measured by using an integrating sphere on a HAMAMATSU Quantaurus-QY C11347-11. TEM images were recorded on a JEM-2100 electron microscope. SEM experiments were performed on the FEI Verios G4 instrument. AFM images were obtained on a Bruker Dimension FastScan and Dimension Icon instrument. PXRD was recorded on a SHIMADZU XRD-7000 with a Cu Kα X-ray source (λ = 1.540598 Å). PXRD was recorded on a SHIMADZU XRD-7000 with a Cu Kα X-ray source (λ = 1.540598 Å). GIWAXS measurements were performed on a Xeuss 2.0 instrument with a wavelength of 1.54189 Å. The distance from samples to detector is c.a. 154 mm.

Energy levels and frontier molecular orbital diagrams calculations. The optimized structures of **M1, M1/C1** and **M1/C2** were performed on G09 software packages.[2] All of the elements were described by the B3LYP/6-31G(d) basis set. The energy levels of HOMO and LUMO were obtained from optimized geometries. There are no imagery frequencies for the optimized geometries.

Energy distribution calculations. To visually observe the non-covalent interactions between **M1** and **C1-C2**, the IGM methods derived from DFT calculations were applied. The M06-2X functional[3] and mixed basis set (the 6-311G(d) basis set for all atoms) was adopted for all calculations. The DFT-D3 with BJ-damping[4] was applied to correct the

weak interactions to improve the calculation accuracy. Then, the energy distribution mapping of optimized structures with color-mapped IGM isosurfaces graphs of **M1**/**C1** and **M1**/**C2** was obtained.

Stacking model simulation. GFN2-xTB method[5] was used to optimize the stacking structure of **M1**, **2DSP-C1** and **2DSP-C2**. The geometric optimization convergence criterion was set to very tight (energy convergence was 1×10^{-7} Eh, and gradient convergence was 2×10^{-4} Eh·α^{-1}). The analytical linearized Poisson-Boltzmann model was used to account for the solvation effect. The GFN2-xTB calculations were realized by xtb code[6] (version 6.5.0).

Molecular dynamics (MD) simulations. Atomistic molecular dynamics simulations were carried out on GROMACS 2021 software[7] for 50 ns. The general AMBER force field (GAFF) were used for small molecules. The system consisted of 6 molecules and 5000 chloroform. Energy minimization was performed with steepest descent algorithm at tolerance value of 10 kJ/mol/nm. Energy minimization was followed by equilibration with position restrain on protein molecule for 100 ps using NVT ensembles with standard coupling methods. Finally, 50 ns production MD simulation was performed with trajectories generated at a time step of 2 fs and frames saved at every 10 ps.

Mathematical fitting of a temperature-dependent model for supramolecular polymerization processes. The supramolecular polymerization mechanism can be probed *via* temperature-dependent UV–Vis spectra measurements.[8] For **M1**, **M1**/**C1**, and **M1**/**C2**, non-sigmoidal denaturation curves were obtained upon plotting the fraction of aggregated species (α_{agg}) against the temperature (T). In particular, α_{agg} in the chain growth phase is described by using Equation S1:

$$\alpha_{\mathrm{agg}} = \alpha_{SAT}\{1 - \exp[(-h_e)(T - T_e)/RT_e^2]\} \qquad \text{(Equation S1)}$$

h_e is the enthalpy of the supramolecular polymerization process. T_e is the critical chain growth temperature.

The α_{agg} in the nucleation phase is described by using Equation S2:

$$\alpha_{\mathrm{agg}} = K_a^{1/3}\exp\left[(2/3K_a^{-1/3} - 1)h_e(T - T_e)/RT_e^2\right] \qquad \text{(Equation S2)}$$

K_a is the equilibrium constant of the nucleation phase.

In the elongation regime, the number-averaged degree of polymerization, averaged over all active species, $\langle N_n \rangle$, is described by using Equation S3:

$$\langle N_n \rangle = K_a^{-1/2}[\alpha_{agg}/(\alpha_{SAT} - \alpha_{agg})]^{1/2} = K_a^{-1/2} \sqrt{\frac{1-\exp\left(\frac{-h_e(T-T_e)}{RT_e^2}\right)}{\exp\left(\frac{-h_e(T-T_e)}{RT_e^2}\right)}} \quad \text{(Equation S3)}$$

Mathematical fitting of a solvent-dependent model for supramolecular polymerization processes. The supramolecular polymerization mechanism can be probed *via* solvent-dependent UV–Vis spectra measurements.[9] For **M1**, **M1**/**C1**, and **M1**/**C2**, non-sigmoidal denaturation curves were obtained upon plotting the fraction of aggregated species (α_{agg}) against the good solvent volume fraction (f). In particular, α_{agg} is described by using Equation S4:

$$\alpha_{agg} = \frac{x_{tot} - x}{x_{tot}} \quad \text{(Equation S4)}$$

x_{tot} is the dimensionless total concentration of monomers, and x is the dimensionless concentration of monomers.

x_{tot} can be described by using Equation S5:

$$x_{tot} = \sigma^{-1} \sum_{i=1}^{n} i(\sigma x)^i + \sigma^{n-1} \sum_{i=n+1}^{\infty} i x^i \quad \text{(Equation S5)}$$

In this equation, σ is the cooperativity parameter.

In addition, equilibrium constants (K_a) and Gibbs free energy (ΔG_0) are described by using Equations S6 and S7:

$$K_a = \exp(-\Delta G_f/RT) \quad \text{(Equation S6)}$$

$$\Delta G_f = \Delta G + mf \quad \text{(Equation S7)}$$

The dependence of ΔG_f on f is described by the m-value. R is the gas constant, and T is the temperature.

Solving Equations S3–S6 yields the thermodynamic parameters (σ, ΔG, K_e) for the solvent-dependent supramolecular polymerization process.

2. Supplementary Figures

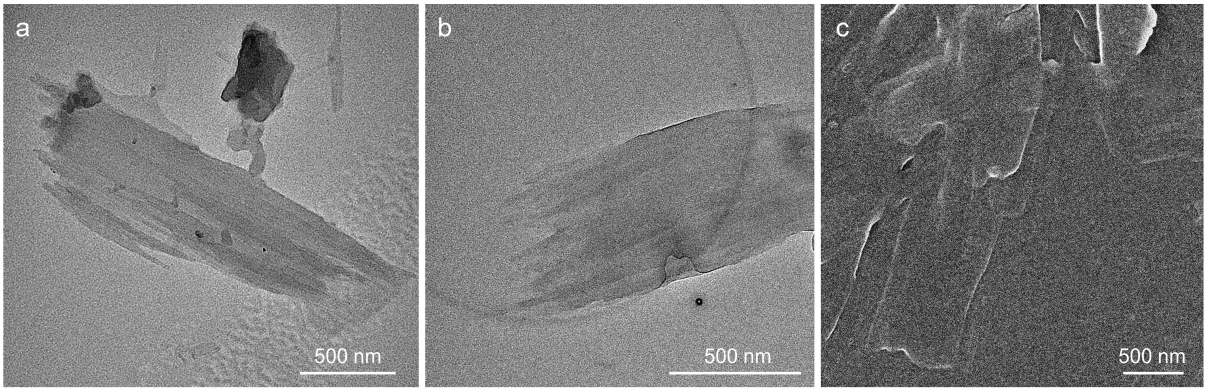

Figure S1. (a) and (b) TEM and (c) SEM images of **2DSP-C1**.

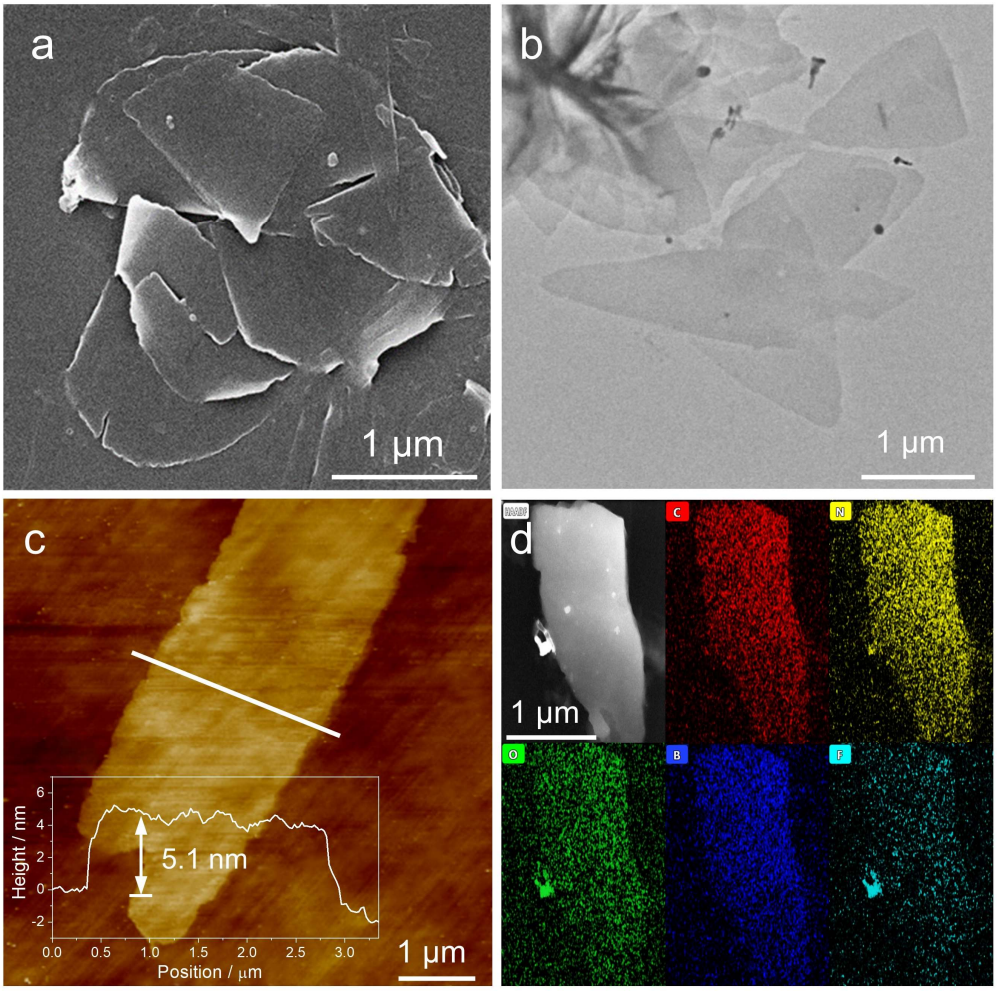

Figure S2. (a) SEM and (b) TEM images of **2DCA-C2**. (c) AFM image and the height profile (inset) of **2DCA-C2**. The height profile of the AFM image along the white lines. (d) HAADF-STEM images and the corresponding EDS for elemental mapping of **2DCA-C2**. The samples of **2DCA-C2** were obtained by slowly evaporating their MCH solution ([**M1**] = [**C2**] = 40 μM and 2 μM for TEM and AFM experiments, respectively).

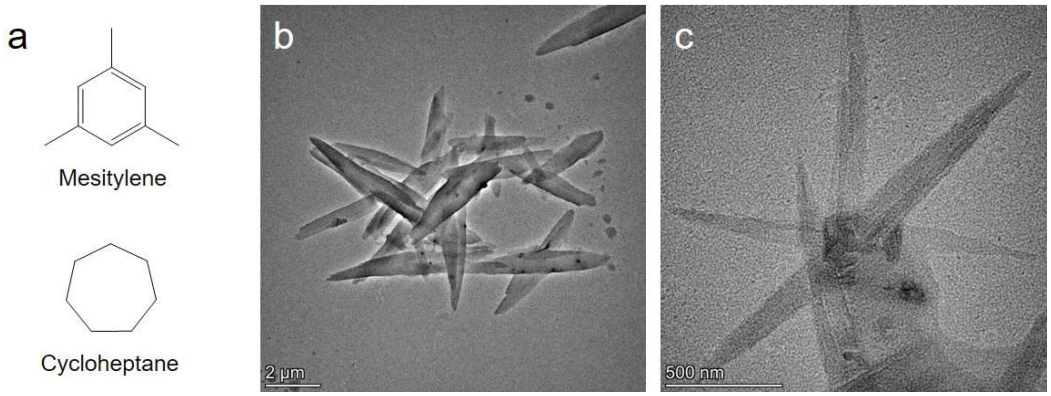

Figure S3. (a) Chemical structures of mesitylene or cycloheptane. (b) and (c) TEM images of the mixture of the equivalent ratio of **M1** with (b) mesitylene and (c) cycloheptane.

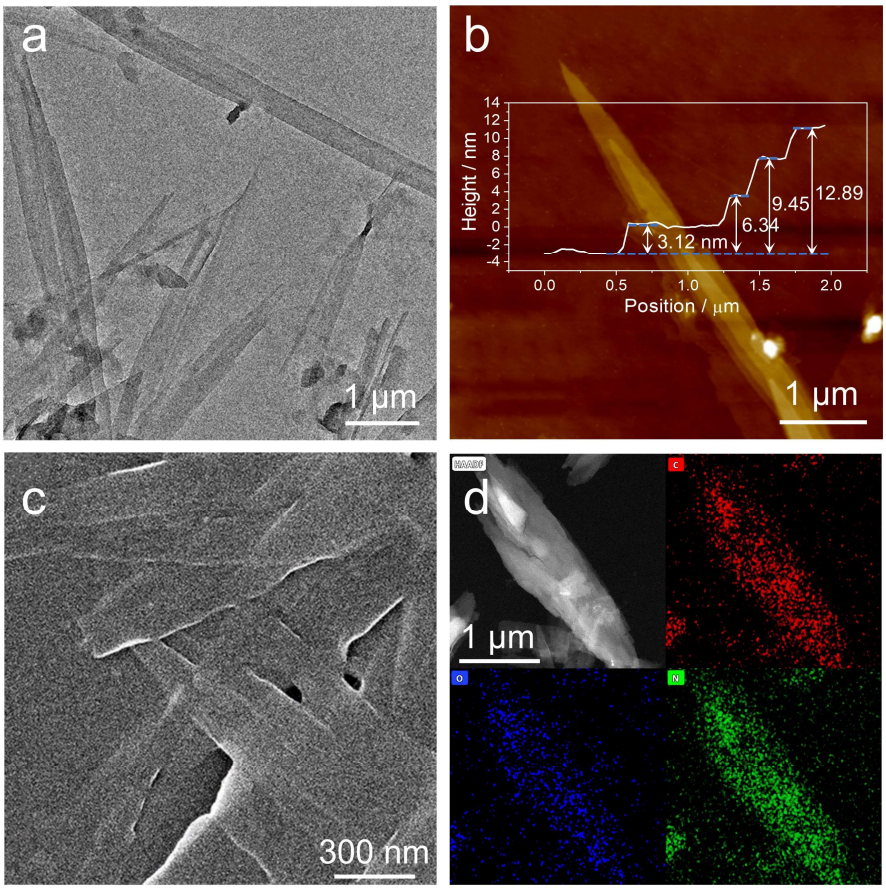

Figure S4. (a) TEM image of **M1**. (b) AFM image and the height profile (inset) of **M1**. The height profiles of AFM images along the white lines. (c) SEM image and (d) HAADF-STEM image and the corresponding EDS mapping of **M1**. 1D spindle-like nanorods were observed for **M1**, which possess a large aspect ratio, and are wide in the middle and narrow at both ends. AFM image showed the multilayer stacking of **M1**. Height profile analysis of the selected area revealed that the average thickness of the thinnest peripheral region is 3.12 nm. EDS mapping showed that the typical elements of C, N and O were uniformly distributed in the sample areas.

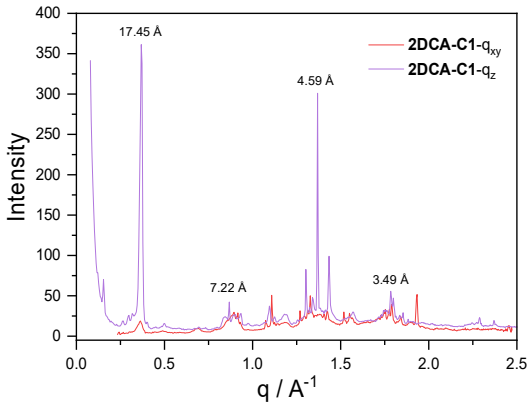

Figure S5. Projections of GIWAXS data of **2DSP-C1** along the q_{xy} axis and q_z axis. Strong diffraction projection signals (q_z = 1.37 and 1.80 Å^{-1}) concentrated near q_{xy} = 0 Å^{-1} were observed, which is consistent with that measured results in PXRD experiments.

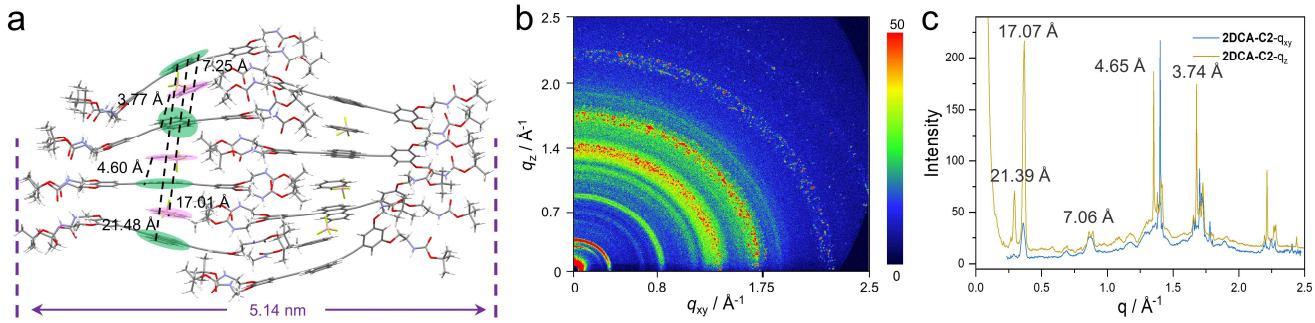

Figure S6. (a) The simulated co-assembly model between **M1** and **C2** via GFN2-xTB method. (b) GIWAXS pattern of **2DSP-C2**. (c) Projections of GIWAXS data along the q_{xy} axis and q_z axis. The simulated stacking length was 5.14 nm, coinciding with the measured thickness in the AFM image. The intensities of out-of-plane (q_z) Bragg peaks were larger than those at in-plane (q_{xy}), reflective of a preferred orientation in the out-of-plane direction. The distances of GIWAXS data were determined to be 21.39, 17.07, 7.06, 4.65, and 3.74 Å, corresponding to the aromatic spacings in the optimized model of **2DSP-C2**.

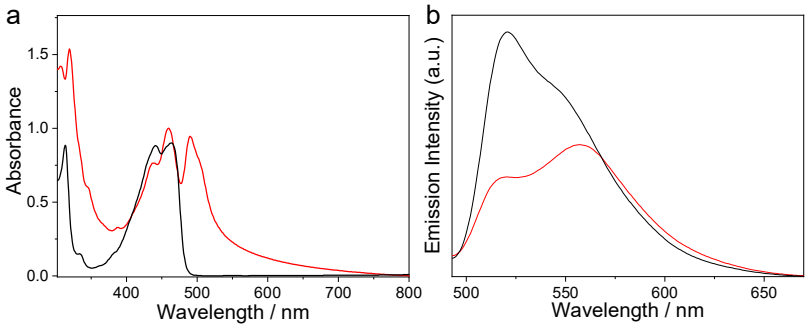

Figure S7. (a) UV–Vis and (b) fluorescence spectra of **M1** in good solvent of $CHCl_3/CH_3OH$ (1 : 1, *v/v*) (black line) and poor solvent of MCH (red line). λ_{ex} = 475 nm.

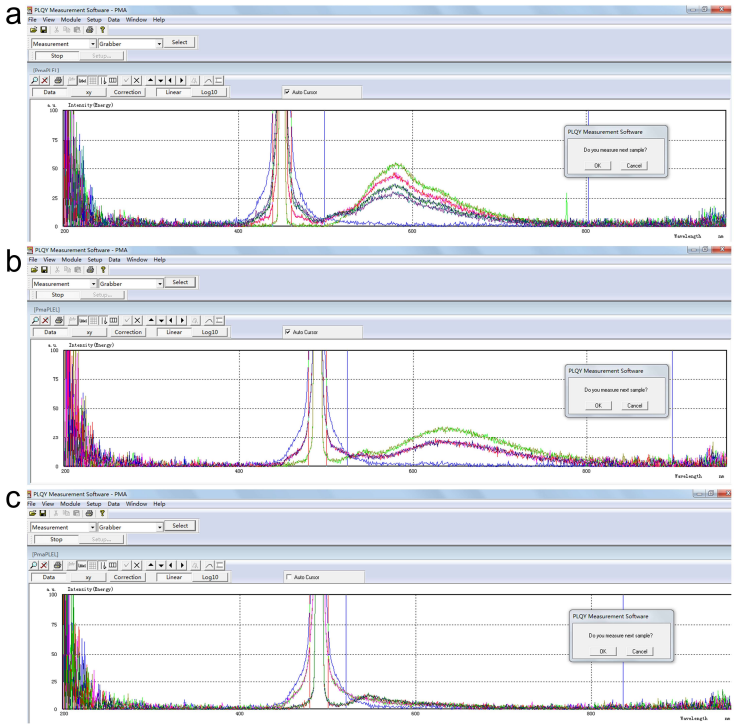

Figure S8. Absolute fluorescence quantum yield of (a) **M1**, Φ_F = 8.93% at 542 nm, (b) **2DCA-C1**, Φ_F = 2.50% at 605 nm and (c) **2DCA-C2**, Φ_F = 1.34% at 550 nm.

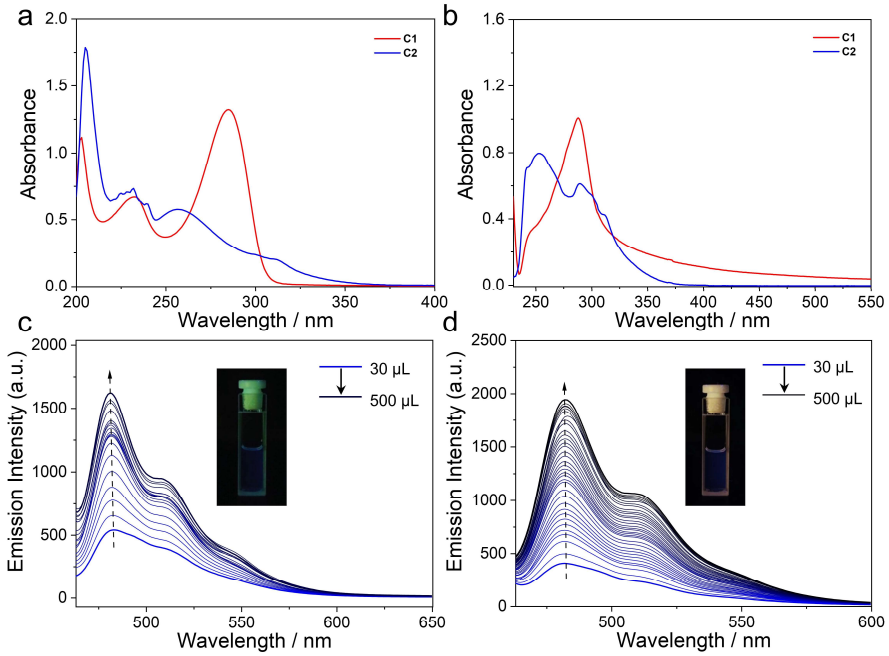

Figure S9. UV–Vis spectra of **C1** and **C2** in (a) good solvent of $CHCl_3/CH_3OH$ (1 : 1, *v/v*) and (b) "poor" solvent of MCH. Fluorescence spectra of (c) **C1** and (d) **C2** in $CHCl_3/CH_3OH$ (1 : 1, *v/v*) with the successive addition of MCH. λ_{ex} = 280 nm. For **C2**, when the proportion of the good solvent ($CHCl_3/CH_3OH$ (1 : 1, *v/v*)) is below ~20%, the gradual addition of the good solvent enhances the solubility of **C2**, increasing its participation in the co-assembly of **2DCA-C2**. Consequently, the self-aggregation tendency of **C2** weakens, accompanied with the reduced blue emission from **C2** and enhanced

yellow emission from **2DCA-C2**. This process results in the apparent red shift emission. Subsequently, when the proportion of the good solvent exceeds ~20%, **2DCA-C2** undergoes de-aggregation, leading to the blue shift in the fluorescence spectra. Compared with **C1**, the fluorescence enhancement of **C2** is large and **2DCA-C2** has a strong fluorescence quenching phenomenon, so it leads to a blue-shifted and then red-shifted effect of **C2** on the fluorescence of **2DCA-C2**.

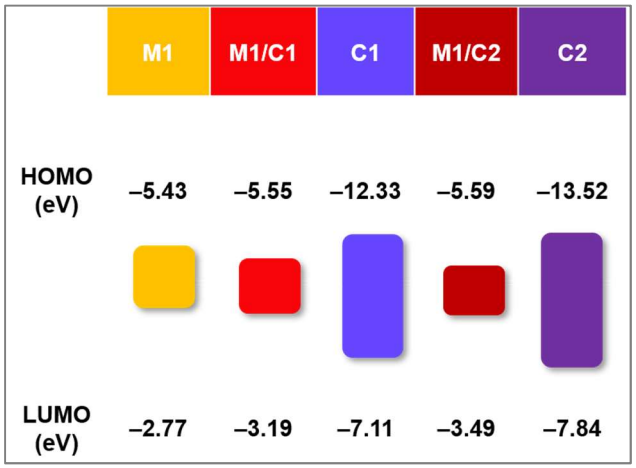

Figure S10. Calculated energy levels of **M1**, **M1**/**C1**, **C1**, **M1**/**C2** and **C2**.

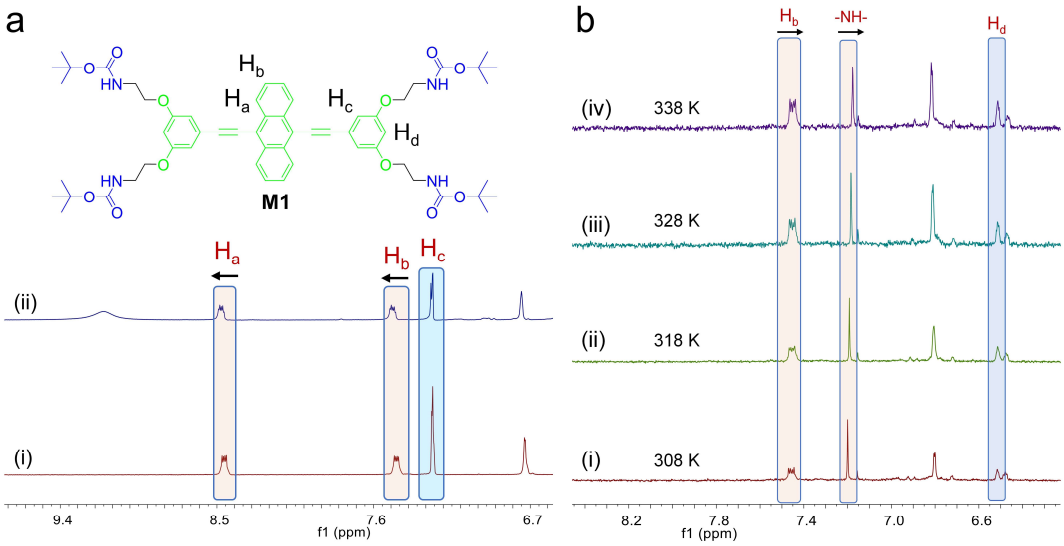

Figure S11. (a) Chemical structure of monomer **M1** and Partial ^{1}H NMR spectra (400 MHz, 298 K) of the high concentration of (i) **M1** (20 mM) and (ii) **M1/C2** (20 mM) in $CDCl_3/CD_3OH$ (2 : 1, *v*/*v*). (b) Temperature-dependent ^{1}H NMR spectra (400 MHz, 2 mM) of **M1/C2** in cyclohexane-d_{12}, (i) 308 K, (ii) 318 K, (iii) 328 K, and (iv) 338 K. As compared to the individual species, downfield of H_a and H_b on **M1** can be observed for an equimolar mixture of **M1** and **C2**, indicating the enhanced electron deficiency for **M1**.

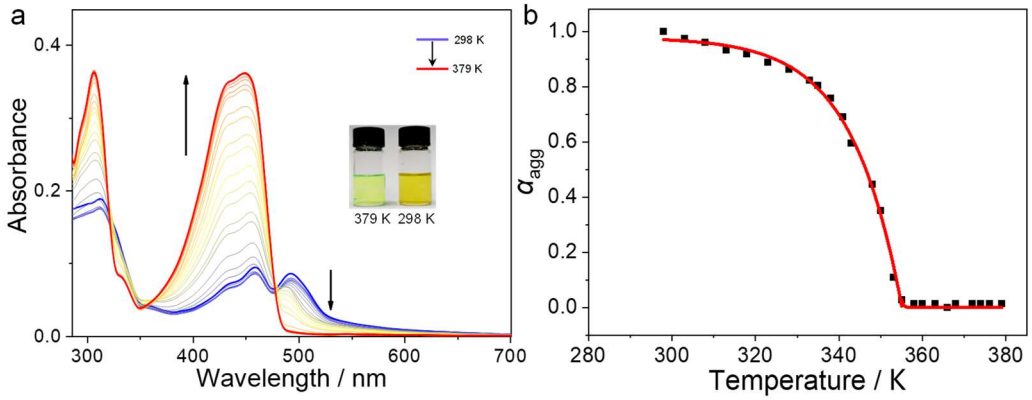

Figure S12. (a) Temperature-dependent UV–Vis spectra variations of **2DSP-C1** and the photographs of **2DSP-C1** at 379 K and 298 K, respectively. (b) α_{agg} values of **2DSP-C1** (10 μM, monitored at λ = 490 nm) versus temperature in MCH. The red line denotes the mathematical fitting curve.

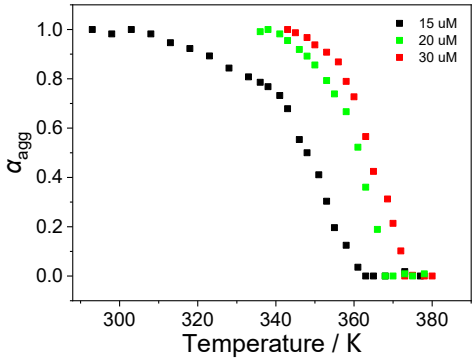

Figure S13. α_{agg} values of **2DSP-C1** (15 μM, 20 μM and 30 μM) monitoring at λ = 490 nm versus temperature in MCH.

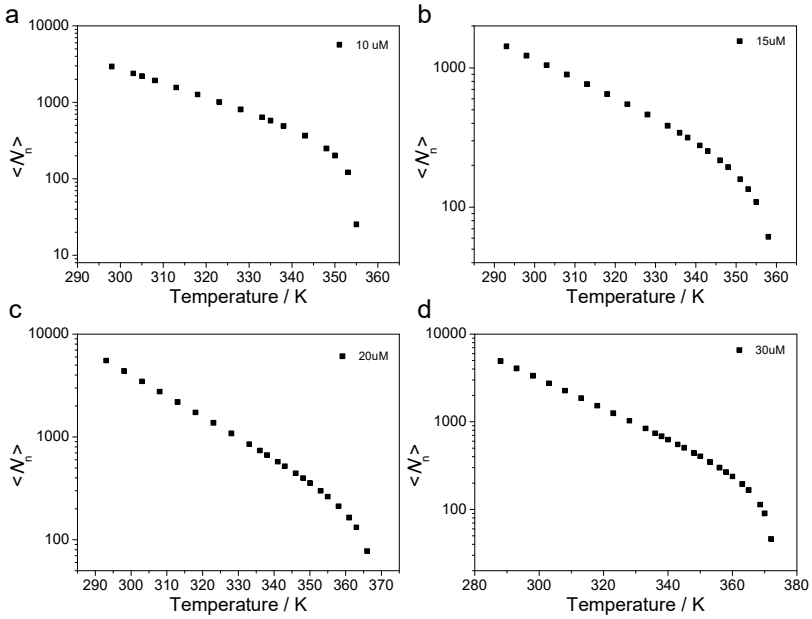

Figure S14. Number-averaged degree of polymerization, averaged over all active species, <N_n> of **2DSP-C1** based on the temperature-dependent absorption data. Concentration: (a) 10 μM, (b) 15 μM, (c) 20 μM, and (d) 30 μM.

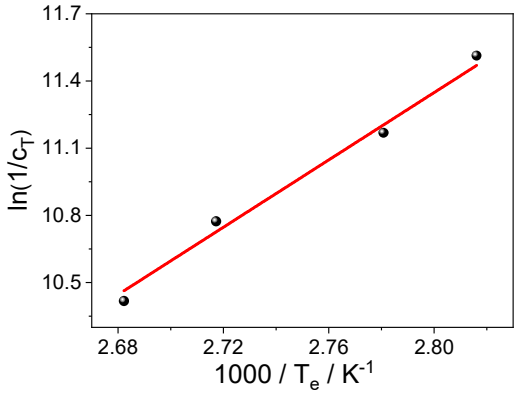

Figure S15. Van't Hoff plot of **2DSP-C1**. The red line denotes the linear fitting curve.

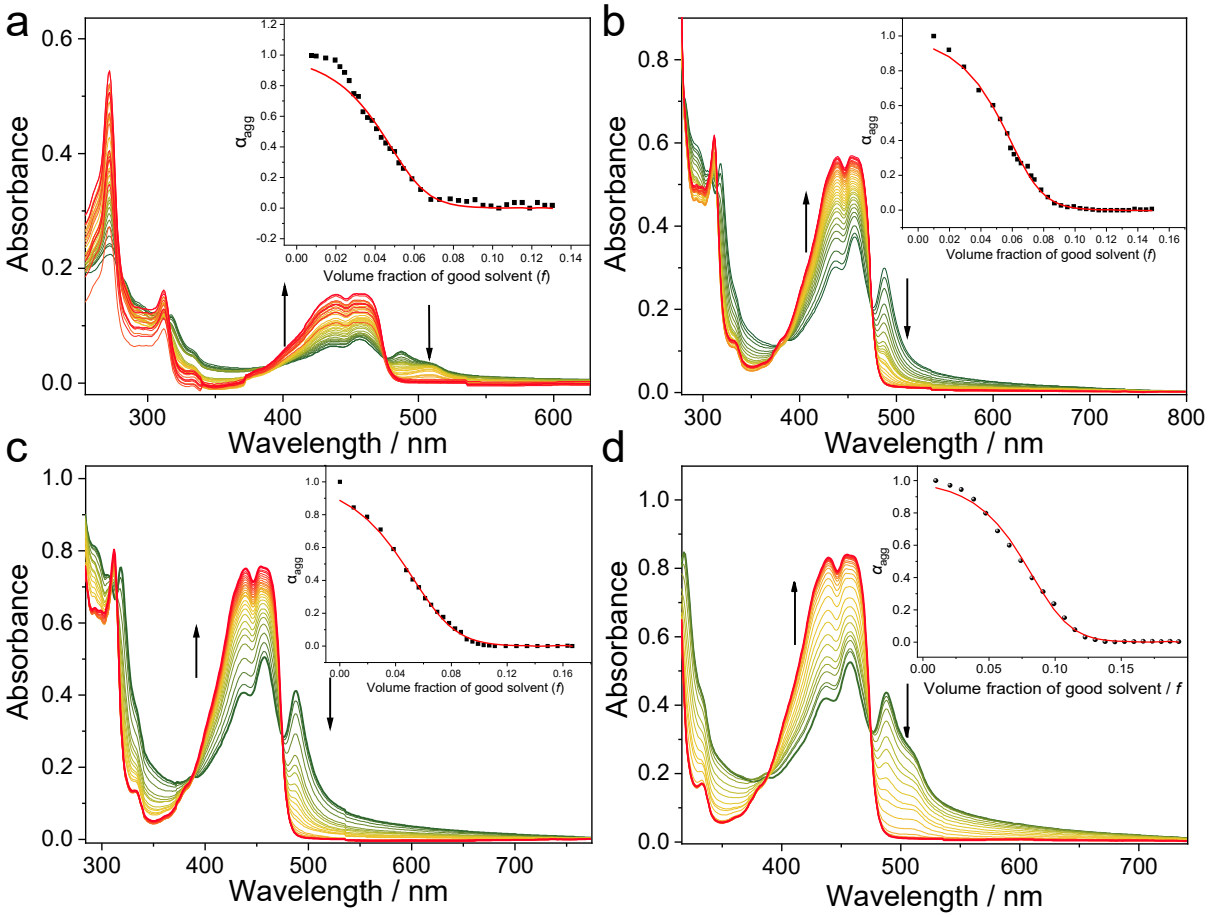

Figure S16. UV–Vis spectra of **2DSP-C1** in MCH upon gradually adding the isoconcentration $CHCl_3/CH_3OH$ (1 : 1, *v*/*v*) solution of **2DSP-C1**. The arrows indicate the spectral variations upon increasing the $CHCl_3/CH_3OH$ (1 : 1, *v*/*v*) volume fraction (*f*). Insets: α_{agg} values of **2DSP-C1** (monitored at λ = 489 nm) *versus f*. The red lines denote the cooperative fitting curves. Concentration: (a) 10 μM, (b) 20 μM, (c) 30 μM, and (d) 40 μM.

Table S1. Thermodynamic parameters for the supramolecular polymerization process of **2DSP-C1**, determined by modeling the temperature- and solvent-dependent UV–Vis spectra data

c (μM)	h_e (kJ mol^{-1})	T_e (K)	K_a	<N_n>[a]	ΔG (kJ mol^{-1})[b]	ΔG (kJ mol^{-1})[c]
10	–86.7	355.1	1.3×10^{-5}	~2900	–38.4	–36.0
15	–65.0	359.6	2.7×10^{-5}	~1200		
20	–104.2	368.0	3.4×10^{-5}	~4300		
30	–89.9	372.8	5.6×10^{-5}	~3300		

[a]Monitoring at 298 K, [b]Obtaining from Van't Hoff plot. [c]Obtaining from solvent-dependent UV–Vis spectra fitting.

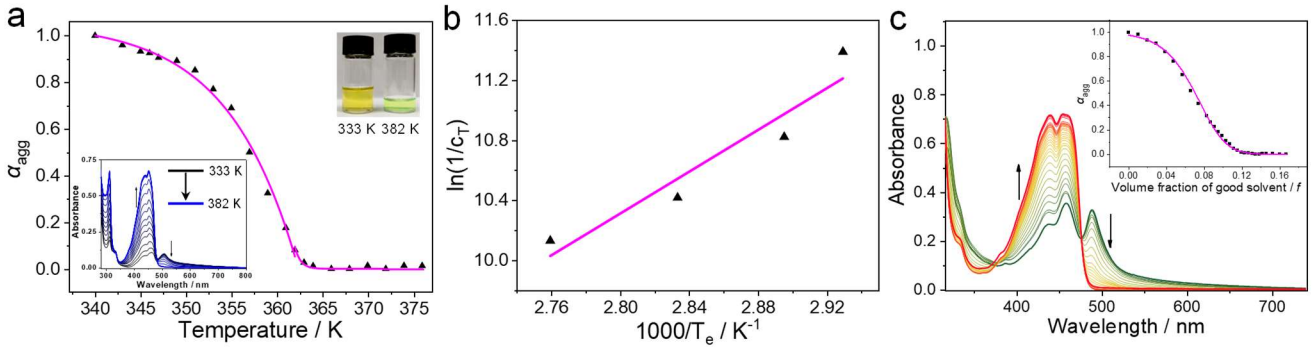

Figure S17. (a) α_{agg} values of **2DSP-C2** (40 μM, monitored at λ = 510 nm) versus temperature in MCH. The pink line denotes the mathematical fitting curve. Insets: temperature-dependent UV–Vis spectra variations of **2DSP-C2** and the photographs of **2DSP-C2** at 333 K and 382 K, respectively. (b) Van't Hoff plot of 2DSP-C2. The pink line denotes the linear fitting curve. (c) UV–Vis spectra of **2DSP-C2** in MCH upon gradually adding the isoconcentration $CHCl_3/CH_3OH$ (1 : 1, *v/v*) solution of **2DSP-C2**. The arrows indicate the spectral variations upon increasing the $CHCl_3/CH_3OH$ (1 : 1, *v/v*) volume fraction (*f*). Insets: α_{agg} values of **2DSP-C2** (monitored at λ = 489 nm) *versus f*. The pink lines denote the cooperative fitting curves.

Table S2. Thermodynamic parameters for the supramolecular polymerization process of **2DSP-C2**, determined by modeling the temperature- and solvent-dependent UV–Vis spectra data

c (μM)	h_e (kJ mol^{-1})	T_e (K)	K_a	<N_n>[a]	ΔG (kJ mol^{-1})[b]	ΔG (kJ mol^{-1})[c]
10	–71.9	341.3	1.6×10^{-4}	~330	-35.1	-37.0
20	–76.5	345.4	5.5×10^{-4}	~200		
30	–36.7	352.9	6.1×10^{-4}	~100		
40	–143.0	362.4	8.7×10^{-4}	~380		

[a]Monitoring at 310 K, [b]Obtaining from the Van't Hoff plot. [c]Average value obtained from the solvent-dependent UV–Vis spectra fitting.

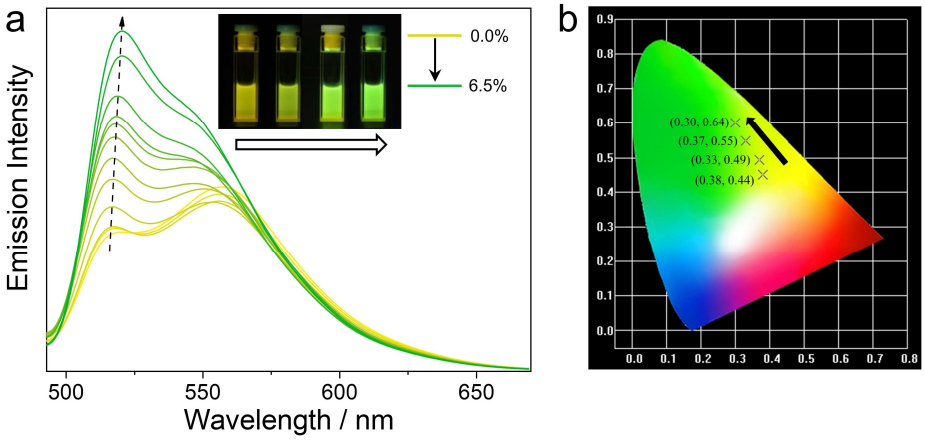

Figure S18. (a) Fluorescence spectra variations of the MCH solution of **M1** (40 μM, λ_{ex} = 475 nm) upon gradually adding the isoconcentration $CHCl_3/CH_3OH$ (1 : 1, *v/v*) solution of **M1**. Inset: selected fluorescence photographs of **M1** in gradually varied solution conditions. (b) The corresponding CIE chromaticity diagrams of **M1**. With the addition of isoconcentration $CHCl_3/CH_3OH$ (1 : 1, *v/v*) solution into the MCH solution of **M1**, the intensity of emission band at 517 nm gradually increased and redshifted. The emission color changed from yellow to green in turn. The corresponding CIE coordinates also showed this trend, ranging from (0.38, 0.44) to (0.30, 0.64).

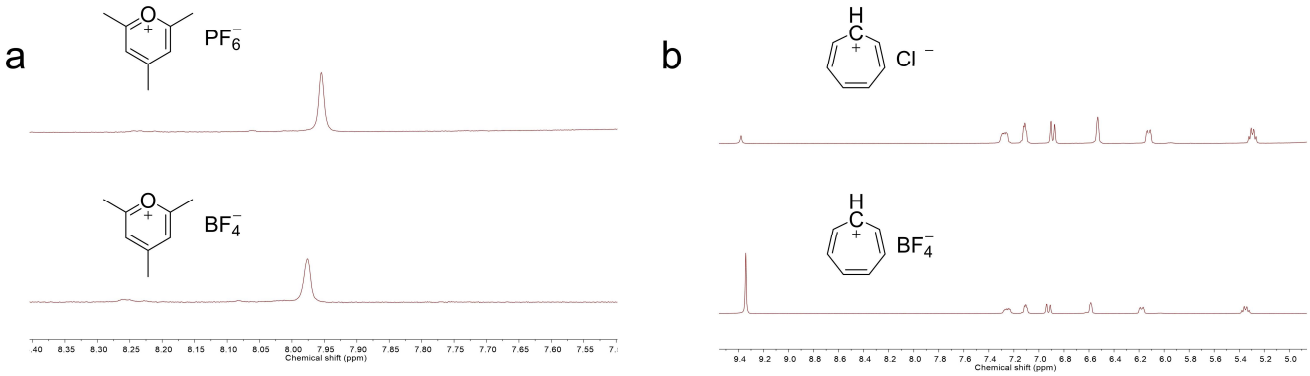

Figure S19. ^{1}H NMR spectra (400 MHz, 298 K) of (a) **C1**-PF_6^- (up) and **C1**-BF_4^- (down), and (b) **C2**-Cl^- (up) and **C2**-BF_4^- (down) in DMSO-*d*$_6$.

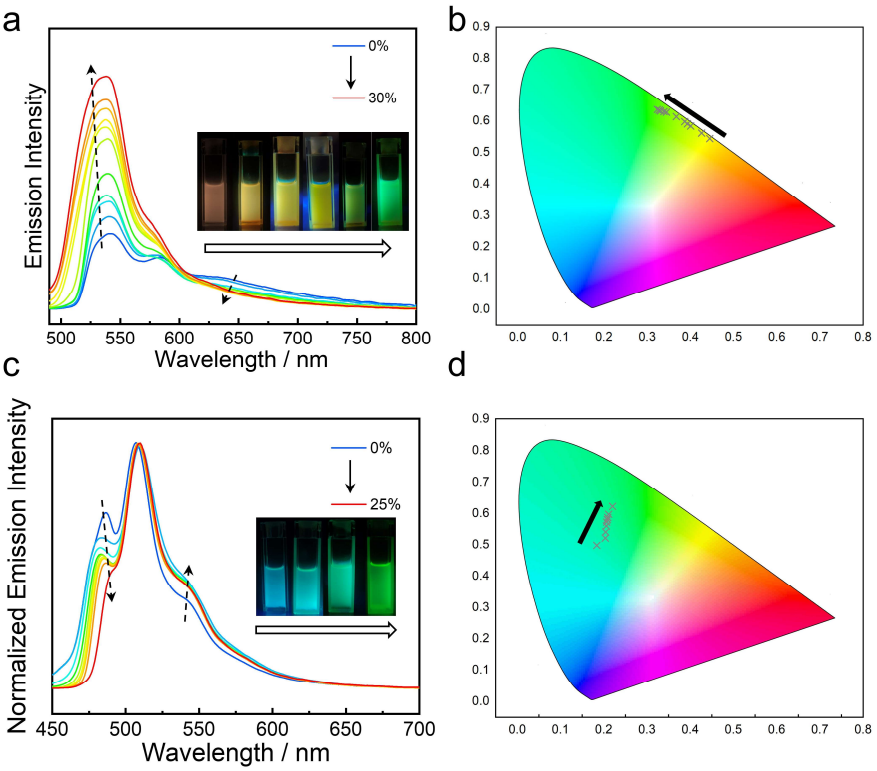

Figure S20. Fluorescence spectra variations of the MCH solution of (a) **2DCA-C1**-PF_6^- (40 μM, λ_{ex} = 490 nm) and (c) **2DCA-C2**-Cl^- (40 μM, λ_{ex} = 440 nm) upon gradually adding the isoconcentration $CHCl_3/CH_3OH$ (1 : 1, *v/v*) solution of **2DCA-C1**-PF_6^- and **2DCA-C2**-Cl^-, respectively. The corresponding CIE chromaticity diagrams of (b) **2DCA-C1**-PF_6^- and (d) **2DCA-C2**-Cl^-.

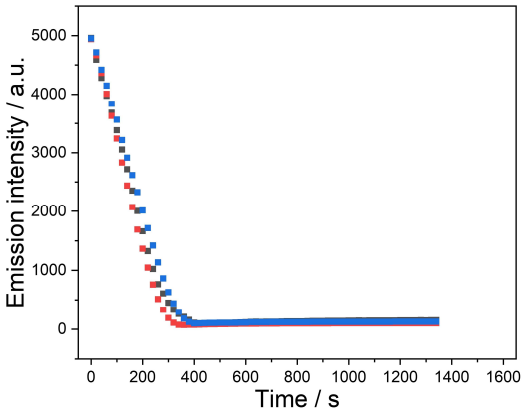

Figure S21. Fluorescence spectra change of the prepared **2DCA-C1** samples (21.5 mg, 2 mg/mL) versus the volatilization time of good solvent of $CHCl_3/CH_3OH$ (1 : 1, *v/v*) at room temperature. The color dots represent three repeated experiments.

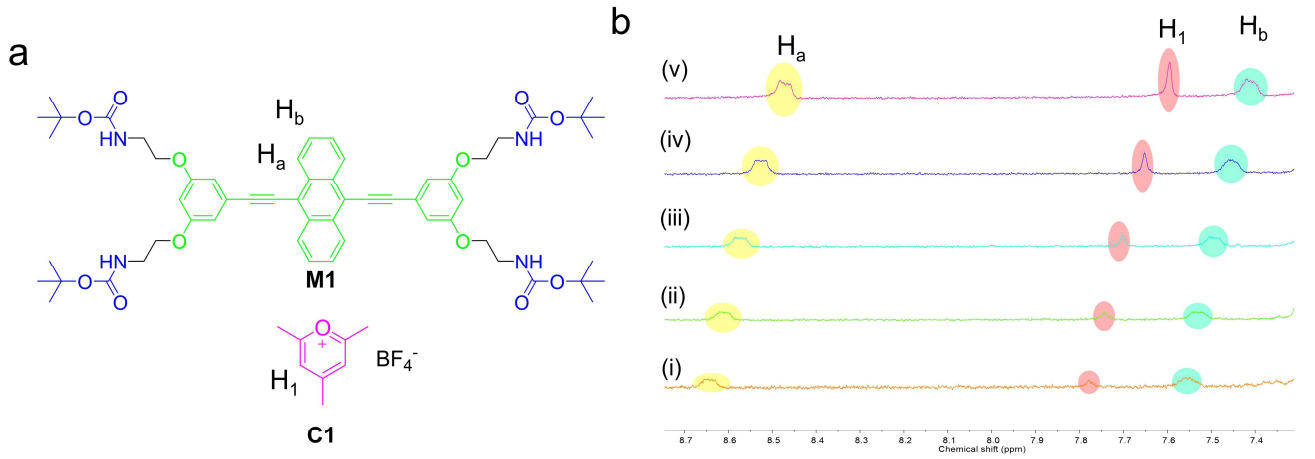

Figure S22. (a) Chemical structure of **M1** and **C1**. (b) Partial ^{1}H NMR spectra (400 MHz, 298 K, 4mM) of the equimolar ratio of **M1** and **C1** in the mixed solution of cyclohexane-d_{12} and $CDCl_3/CD_3OH$ (1 : 1, *v/v*). cyclohexane-d_{12} : $CDCl_3/CD_3OH$ (1 : 1, *v/v*) = (i) 475 : 25, (ii) 475 : 50, (iii) 475 : 75, (iv) 475 : 100, (iv) 475 : 125.

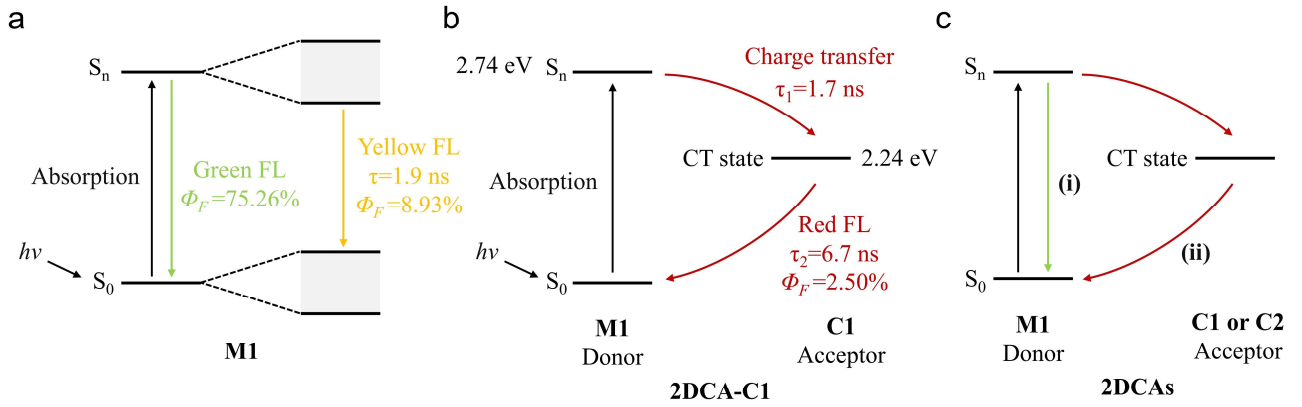

Figure S23. Schematic representation of the involved photo-physics pathways of (a) **M1**, (b) **2DCA-C1**, and (c) the effect of solvent vapor on the multifluorescence tunable features. For **M1** in the self-assembled state, due to the π-electron delocalization induced reduction of energy level between ground state and excited state, a redshifted and weaker yellow emission is observed compared to its stronger green emission in the molecular dissolved state. Therefore, upon adding good solvent into the self-assembled **M1**, the yellow emission gradually changes to green emission with the de-aggregation of the self-assembled **M1**. For **2DCA-C1**, it passes from the excited state (S_n) through the CT state until falls back to the ground state (S_0), showing a more redshifted red emission compared to **M1**. Benefit from the trade-off of the process (i) and (ii), the multifluorescent tunable photo-physics pathways is realized.

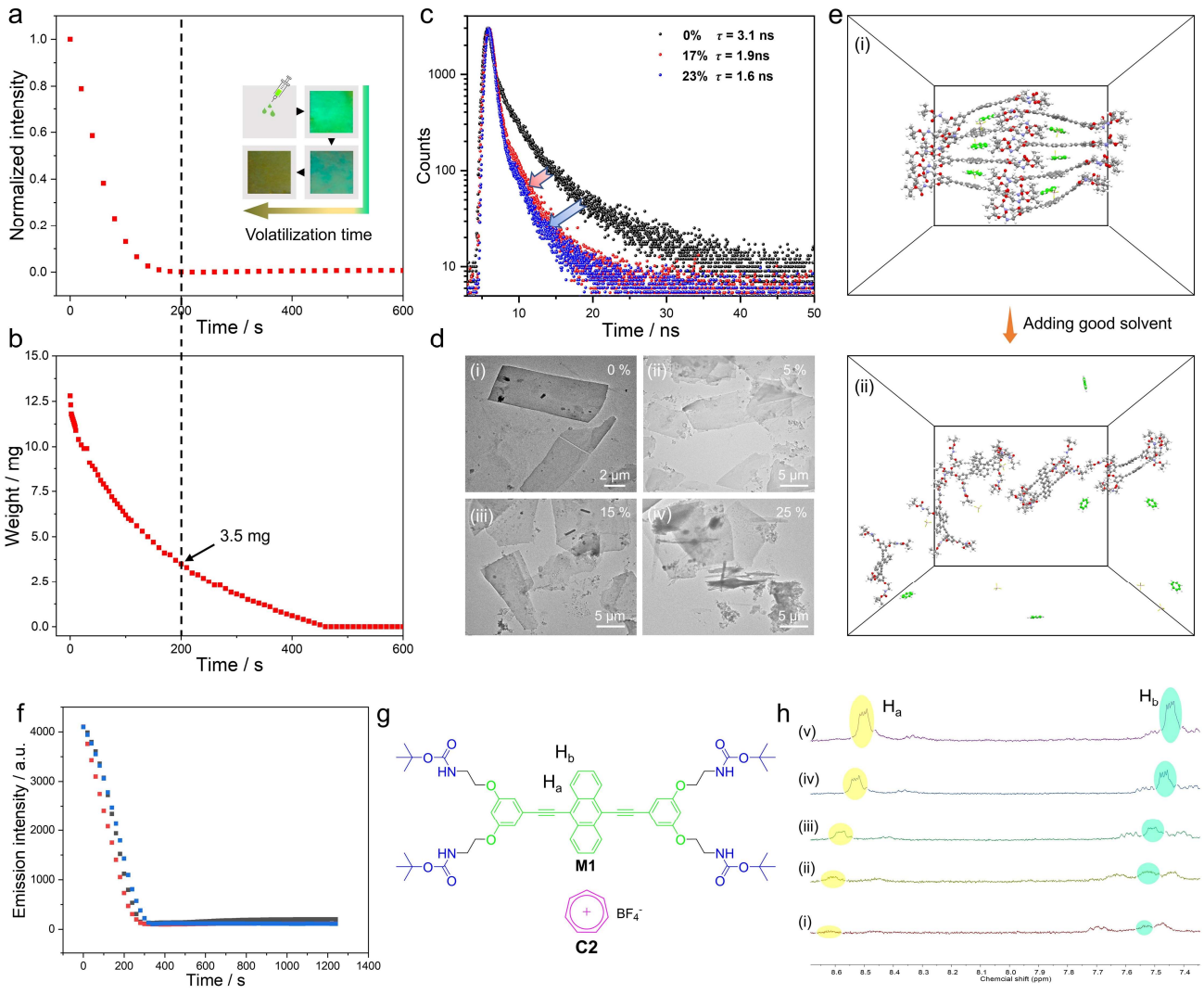

Figure S24. (a) Fluorescence spectra and (b) the corresponding weight variation of **2DCA-C2** versus the volatilization time of good solvent of $CHCl_3/CH_3OH$ (1 : 1, *v/v*) at room temperature. Inset of (a): schematic illustration of the sample preparation for quantitatively determining the molar stoichiometry of $CHCl_3/CH_3OH$ (1 : 1, *v/v*) in the vapo-fluorochromic experiments. (c) Fluorescence decay profiles of **2DCA-C2** in MCH upon addition of 0%, 17%, and 23% volume of $CHCl_3/CH_3OH$ (1 : 1, *v/v*). (d) TEM images of **2DSP-C2** in MCH upon addition of (i) 0%, (ii) 5%, (iii) 15%, and (iv) 25% volume of $CHCl_3/CH_3OH$ (1 : 1, *v/v*). (e) The stacking modes of **2DCA-C2** (i) in benzene and (ii) in $CHCl_3/CH_3OH$ (1 : 1, *v/v*) obtained from MD simulations at the final snapshots. (f) Fluorescence spectra change of the prepared **2DCA-C2** samples (21.7 mg, 2 mg/mL) versus the volatilization time of good solvent of $CHCl_3/CH_3OH$ (1 : 1, *v/v*) at room temperature. The color dots represent three repeated experiments. (g) Chemical structure of **M1** and **C2**. (b) Partial ^{1}H NMR spectra (400 MHz, 298 K) of the equimolar ratio of **M1** and **C2** in the mixed solution of cyclohexane-d_{12} and $CDCl_3/CD_3OH$ (1 : 1, *v/v*). cyclohexane-d_{12} : $CDCl_3/CD_3OH$ (1 : 1, *v/v*) = (i) 400 : 25, (ii) 400 : 50, (iii) 400 : 75, (iv) 400 : 100, (v) 400 : 125.

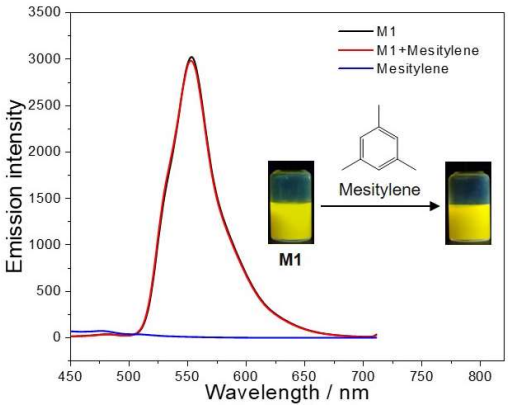

Figure S25. Fluorescence spectra of **M1**, **M1**+mesitylene, and mesitylene in MCH.

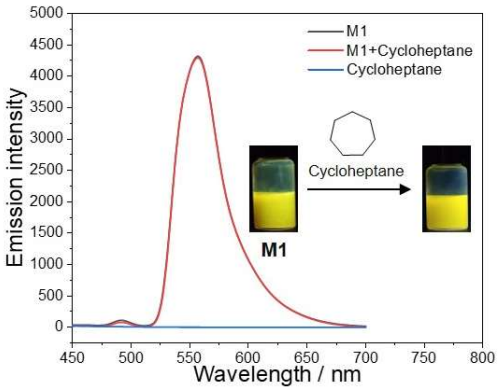

Figure S26. Fluorescence spectra of **M1**, **M1**+cycloheptane, and cycloheptane in MCH.

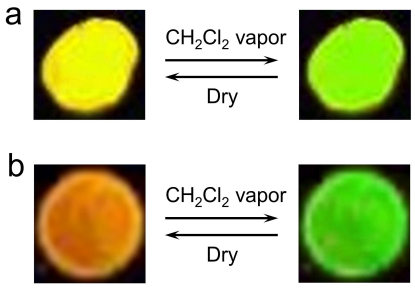

Figure S27. The reversible vapor-responsiveness of (a) **M1** and (b) **2DSP-C1**.

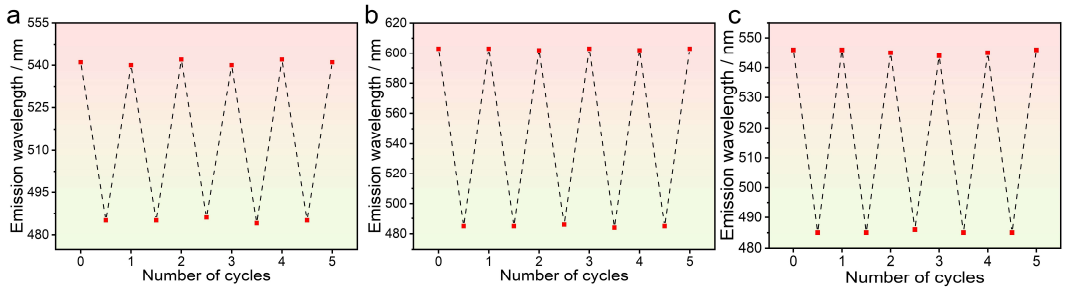

Figure S28. Fluorescence wavelength of the solids of (a) **M1**, (b) **2DCA-C1** and (c) **2DCA-C2** upon successively fuming with good solvent vapor and drying at room temperature. The emission could withstand at least five cycles while retaining their original properties, indicating the favorable reversibility.

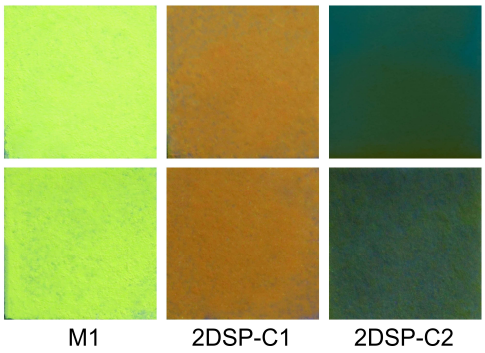

Figure S29. Photographs of the 3D codes units on one day (up) and after two months (down). The pattern derived from **M1**, **2DSP-C1** and **2DSP-C2** possess enough stability, as evidenced by unchanging of the emission color under the ambient conditions for at least two months.

3. Synthetic routes to the targeted monomer

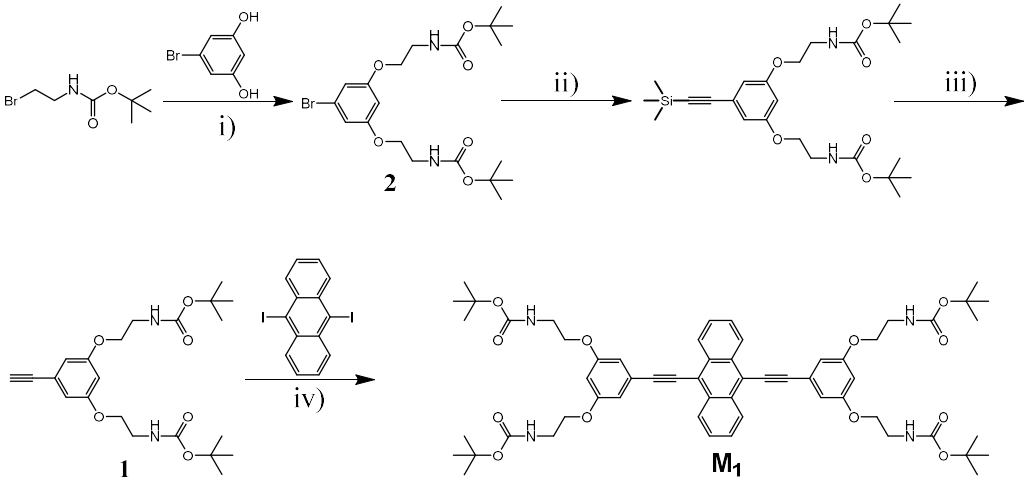

Figure S30. Synthetic routes to the targeted monomers **M1**. i) K_2CO_3, KI, DMF; ii) Trimethylsilylacetylene, $Pd(PPh_3)_2Cl_2$, CuI, PPh_3, TEA; iii) K_2CO_3, KOH, MeOH, THF, H_2O; iv) $Pd(PPh_3)_2Cl_2$, CuI, PPh_3, TEA. The synthetic routes were similar to our previously reported work.[10]

3.1 Synthesis of compound 2

Compound 5-bromoresorcinol (1.2 g, 6.36 mmol), K_2CO_3 (1.77 g, 12.70 mmol) and KI (1.1 g, 6.48 mmol) were mixed in 25 mL of DMF and stirred under nitrogen atmosphere. And tert-butyl (2-bromoethyl)carbamate (3.6 g, 16.07 mmol) was then added dropwise to the reaction mixture over 30 minutes. The reaction mixture was stirred overnight at 60°C, then extracted three times with H_2O and CH_2Cl_2. The combined organic layers were dried over anhydrous Na_2SO_4, and the solvent was removed using a rotary evaporator. The residue was purified via flash column chromatography using petroleum ether/ethyl acetate (20:1, *v*/*v*) as the eluent to afford **2** as light yellow oily liquid (2871.3 mg, 95.0 %).^{1}H NMR (400 MHz, $CDCl_3$) δ (ppm): 6.66 (d, J = 1.9 Hz, 2H), 6.37 (s, 1H), 4.95 (s, 2H), 3.97 (t, J = 5.0 Hz, 4H), 3.54–3.47 (m, 4H), 1.45 (s, 18H).

3.2 Synthesis of compound 1

Compound **2** (375.3 mg, 0.80 mmol), $Pd(PPh_3)_2Cl_2$ (201.8 mg, 0.29 mmol) , CuI (54.3 mg, 0.29 mmol) and PPh_3 (75.2 mg, 0.29 mmol) were mixed in 20 mL of TEA and

stirred under nitrogen atmosphere. Trimethylsilylacetylene (386.6 mg, 3.95 mmol) was added dropwise to the reaction mixture over 30 minutes. After stirring at 55 ºC for 12 hours, the reaction mixture was concentrated to remove the solvent. The resulting residue was then purified using flash column chromatography with petroleum ether/ethyl acetate (10:1, *v*/*v*) as the eluent, yielding the product as a light yellow solid (209.9 mg, 80.5%). The resulting compound was treated with K_2CO_3 (491.4 mg, 3.56 mmol) and KOH (199.5 mg, 3.56 mmol) in THF/MeOH/H_2O (25 mL, 2:2:1, *v*/*v*) at 28°C for 6 hours. After the deprotection reaction, the solvent was removed in vacuo, and the residue was extracted with H_2O and CH_2Cl_2. The combined organic layers were dried over anhydrous Na_2SO_4, and the solvent was removed via rotary evaporation. The residue was purified again by flash column chromatography (petroleum ether/ethyl acetate, 10:1, *v*/*v*) to obtain compound **1** as a white solid (240.2 mg, 71.8%).^{1}H NMR (400 MHz, $CDCl_3$) δ (ppm): 6.63 (d, J = 1.8 Hz, 2H), 6.45 (s, 1H), 4.96 (s, 2H), 3.98 (t, J = 4.9 Hz, 4H), 3.55–3.48 (m, 4H), 3.04 (s, 1H), 1.45 (s, 18H).

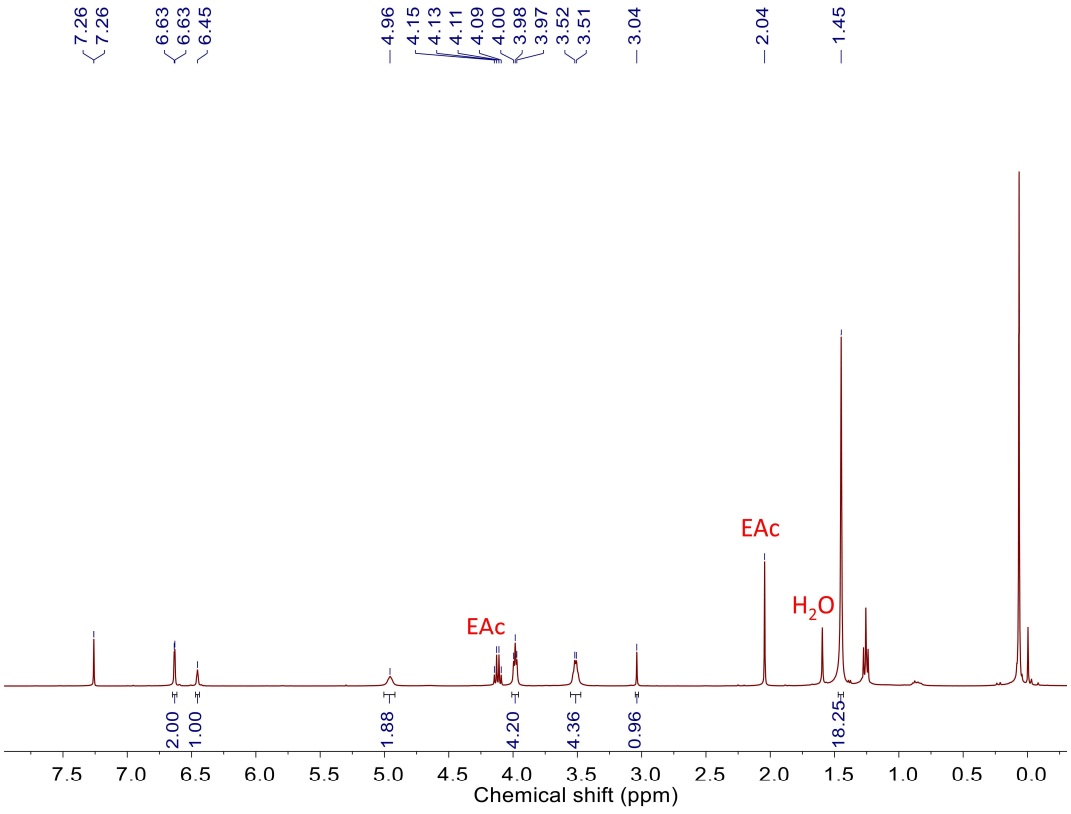

Figure S31. ^{1}H NMR spectrum (400 MHz, $CDCl_3$, 298 K) of **1**.

3.3 Synthesis of compound M1

9,10-Diiodoanthracene (100.6 mg, 0.24 mmol), compound **1** (244.4 mg, 0.58 mmol), $Pd(PPh_3)Cl_2$ (63.6 mg, 0.10 mmol) and CuI (61.8 mg, 0.34 mmol) were mixed in TEA (20 mL) and stirred under nitrogen atmosphere. The mixture was stirred at 75°C for 12 hours, after which the solvent was evaporated, and the residue was extracted three times with H_2O and CH_2Cl_2. The combined organic layers were dried over anhydrous Na_2SO_4, filtered under reduced pressure, and the solvent was removed using a rotary evaporator. The residue was washed three times with triethylamine and then placed under vacuum at 50°C for 12 hours. The resulting solid was cooled to room temperature to yield **M1** as a yellowish solid (184.1 mg, 75.6%).^{1}H NMR (400 MHz, $CDCl_3$) δ (ppm): 8.66 (dd, J = 6.6, 3.2 Hz, 4H), 7.66 (dd, J = 6.7, 3.2 Hz, 4H), 6.92 (d, J = 1.8 Hz, 4H), 6.54 (s, 2H), 5.03 (s, 4H), 4.10 (t, J = 4.7 Hz, 8H), 3.66–3.52 (m, 8H), 1.47 (s, 36H).

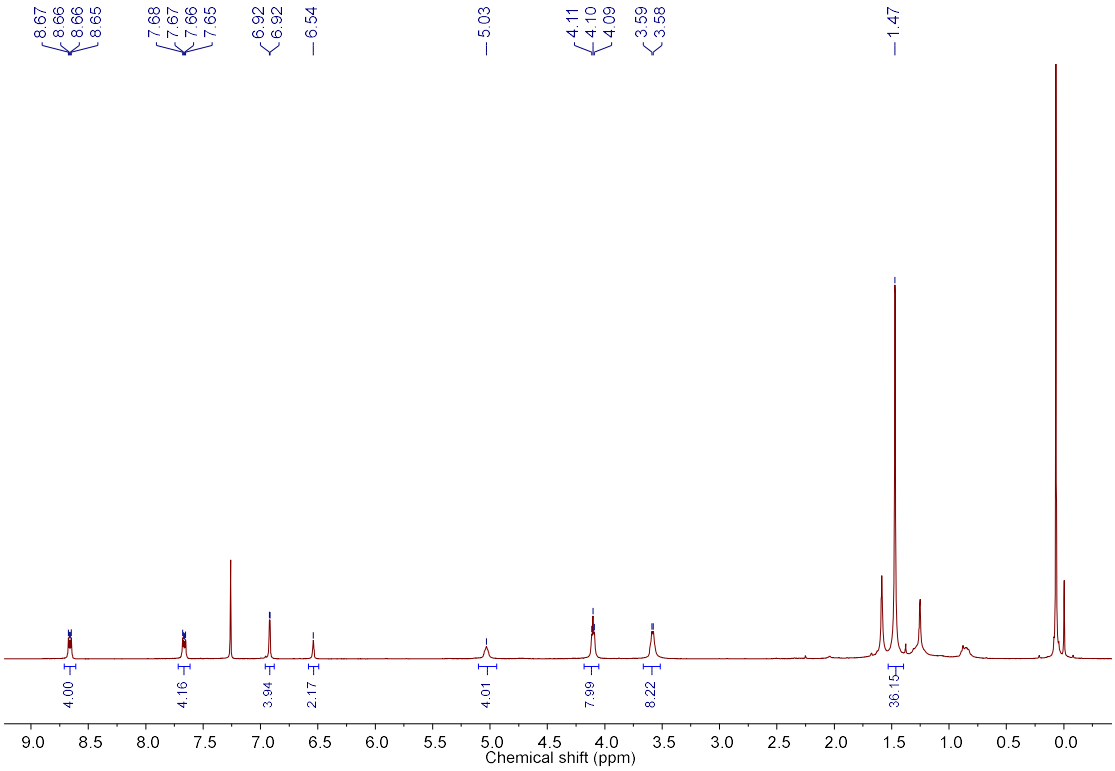

Figure S32. ^{1}H NMR spectrum (400 MHz, $CDCl_3$, 298 K) of **M1**.

4. References

[1] M. Lübtow, I. Helmers, V. Stepanenko, R. Q. Albuquerque, T. B. Marder and G. Fernández, *Chem. Eur. J.* 2017, **23**, 6198.

[2] Frisch, M. J. et al. Gaussian 09, Revision D.01 (Gaussian, Inc., Wallingford CT, 2013).

[3] Y. Zhao and D. G. Truhlar, *Theor. Chem. Acc.,* 2008, **120**, 215–241.

[4] S. Grimme, S. Ehrlich and L. Goerigk, *J. Comp. Chem.,* 2011, **32**, 1456–1465.

[5] S. Grimme, C. Bannwarth, P. Shushkov, *J. Chem. Theory Comput.* 2017, **13**, 1989–2009.

[6] C. Bannwarth, E. Caldeweyher, S. Ehlert, A. Hansen, P. Pracht, J. Seibert, S. Spicher and S. Grimme, *WIREs Comput. Mol. Sci.,* 2021, **11**, e1493.

[7] B. Hess, C. Kutzner, D. van der Spoel, and E. Lindahl, *J. Chem. Theory Comput.,* 2008, **4**, 435–447.

[8] M. M. J. Smulders, A. P. H. J. Schenning, and E. W. Meijer, J. *Am. Chem. Soc.* 2008, **130**, 606–611.

[9] P. A. Korevaar, C. Schaefer, T. F. A. de Greef, and E. W. Meijer, *J. Am. Chem. Soc.* 2012, **134**, 13482–13491.

[10] Z. Gao, J. Sun, L. Shi, W. Yuan, H. Yan and W. Tian, *Angew. Chem. Int. Ed.* 2025, **64**, e202423174.